Response to Referee #1:

l. 87: The reader could wonder where these labels are coming from. The Authors could put a brief link to Sec. 2.2 in anticipation of this question.

Great idea! I can add that in.

Sec. 2.1: Please list the pixel size and the orbit of the satellite. Can sun-glint be expected?

The pixel size of the Hyperion instrument is 30 m per pixel and 7.5 km by 100 km land area per image. It followed a polar orbit.

l. 100: Please briefly mention the selection process of 102 sample maps. How important is coverage across solar geometries versus surface types?

To ensure that we sampled the entire globe, we collected approximately 25 images from each section of the globe. Namely the Arctic, Northern Midlatitude, Tropics, Southern Midlatitude, and Antarctic. We found that there were many less applicable images from both of the polar regions so combining them we included 21 images. We found that there were many Tropic images so that sample set ending up being 30 images and the Midlatitudes add up to 51. These number are not round because of the issue of resampling when including the Ocean subset. The 19 in the ocean category can be found in the other latitudinal zones, so any cross over between the two subsets were eliminated to ensure the entire sample set was unique.

Since we worked with TOA brightness, we did not need to consider solar geometries. According to our study of cloud brightness by latitude, surface type does play a role in apparent cloud brightness so it was important for us to include a variety of latitudinal ranges.

ll. 106-109: The purpose of this sentence is not apparent. Please rephrase or exclude if irrelevant.

The purpose of these sentences is to inform readers about the selection of three bands to classify cloudy pixels. It gives background to the radiation sources that the instrument measures. These sentences will be written as: In order to detect cloudy pixels with confidence, we selected three specific spectral bands that can distinguish clouds from other surface types. It is important to note that Earth's total TOA energy flux constitutes the total incoming solar radiation, the consequential outgoing reflected shortwave radiation from the clouds and surface, and the outgoing emitted longwave radiation from Earth's surface, atmosphere, and clouds (e.g., Trenberth et al. 2009).

ll. 117-119: I understand the satellite hardware limits the complexity of a cloud screening algorithm. How much more complex (than decision trees) could a potential algorithm be? What exactly are the limitation: RAM or CPU power? Perhaps these answers could extent the discussion in Sec. 4.

The algorithm that we propose uses pre-calculated thresholds to screen data onboard. This method is of similar complexity to decision trees such that decision trees have N thresholds, where N is the maximum height of the tree, and our process uses 3 thresholds.

Hyperspectral instruments produce data rates of Gb/s and with relatively simple hardware (FPGA), or with hardware that people are starting to fly now (see below) you could keep up. Current efforts to fly more powerful computation include flight of the Qualcomm Snapdragon on the Mars Helicopter [Grip et al. 2019] and flight of the Intel Myriad Chip on FSSCCAT [ESA 2020], however future computing needs for onboard AI will continue to grow [Dally et al. 2020].

Dally, William J., Yatish Turakhia, and Song Han. "Domain-specific hardware accelerators." Communications of the ACM 63.7 (2020): 48-57.

Grip HF, Lam J, Bayard DS, Conway DT, Singh G, Brockers R, Delaune JH, Matthies LH, Malpica C, Brown TL, Jain A. Flight Control System for NASA's Mars Helicopter. In AIAA Scitech 2019 Forum 2019 (p. 1289).

European Space Agency (ESA), FSSCCAT-1 Ready for Launch, https://www.esa.int/Applications/Observing_the_Earth/Ph-sat/FSSCat_F-sat-1_ready_for_launch , retrieved 6 August 2020

For example, EO-1 had a Mongoose M5 which is a variant of a RAD 3000 (PowerPC family) CPU. It had a 6 MHz clock speed so around 6 MIPS processing power. The challenge is that it had no hardware floating point support. If the computation was all performed fixed point it would be much more efficient, but all onboard classification was performed on top of the atmosphere reflectance data which was in floating point. Additionally, it had most but not all of the CPU for image processing. Therefore scenes required 10's of minutes to load into RAM and process, during which time another scene could not be acquired (as the Solid State Recorder could not simultaneously read and write).

Current spacecraft have more computing capability but still fall far below laptop like computing power. A typical flight CPU would be a Rad 750 (about 200 MIPS) with 128 MB RAM. In comparison a typical laptop in 2020 has 400K MIPS or 2000x the compute power and 16 GB RAM. Future spacecraft are likely to have special purpose processors to handle instrument processing that would enable more sophisticated processing onboard. For example, the Mars 2020 Helicopter uses a Qualcomm Snapdragon processor.

ll. 145-146: Should the ‘historical average’ be determined from the same pixel size as the future samples? (or in other words: does cloud fraction change when using larger or smaller pixels?) And what cloud optical thickness threshold was used for MODIS cloud detection? Perhaps the Authors could discuss these answers in the Sec. 4.

We actually did not experiment with how our historical averages change with pixel size. The best I can do to address this concern is point the reviewers to the method we used to label our

ground truth pixels. The pixels surrounding areas of a certain surface type were labeled as ambiguous and not used in our cloud fractions so that any pixels that may include two classification types were not misclassified either way, thus not included in the historical average. This method helps to mitigate any change in cloud fraction where pixel size varies, for example if more than one surface type is present due to the large pixel size. Although, we could complete a study using data with smaller and larger pixels to definitively say that the pixel size is not a large concern, but it fell outside the scope of the study we conducted.

ll. 193-203: Perhaps these paragraphs are better suited for the discussion in Sec. 4.

Thank you for the suggestion, I agree!

ll. 259-262: Perhaps this paragraph is better suited for the discussion in Sec. 4.

Thank you for the suggestion, I agree!

Fig. 2: Please explain the colors in this figure.

Thank you for the suggestion, that would be helpful!

Fig. 5: Which wavelength was used to capture this image? Please add the fraction of excluded pixels in b, c, and d to the caption.

This Hyperion image is named EO1H1940712011304110T1. The image was created using the default RGB wavelengths in the ENVI program, although the algorithm to create the image in this figure only considers the three wavelengths used in our thresholds. The RGB image is used for visualization. The images in b, c and d show the pixels excised based on our calculated thresholds using a false positive of 1000, 100 and 10, respectively. Figure 5b has 8.5% of the total pixels excised, figure 5c has 16.4%, and figure 5d has 25%. I plan to revise the figure caption to include the filename and the percentage of excised pixels.

Response to Referee #2:

1. Section 2.1 (page 4): what is the pixel size of the Hyperion instrument? How do you C1 AMTD Interactive comment Printer-friendly version Discussion paper consider the instrumental differences between Hyperion and EMIT instrument (such as pixel size, wavelength, etc.)?

The pixel size of the Hyperion instrument is 30 m per pixel and 7.5 km by 100 km land area per image. EMIT has a spectral resolution from 380-2510 nm and a spatial resolution of 30 m per pixel, both very similar to Hyperion.

2. Section 2.2 (page 4): it is unclear to me how to manually label the 102 Hyperion images (7.7km x 42km)? Could you please provide more details?

We manually labeled the pixels in each scene using an image editing software called GIMP. In this software we manually labeled pixels by human classification, visually. Depending on the classification, the pixel was given a color (in value); red, green, blue, cyan, or black. Black pixels bordered each other classification type to mitigate misclassifications or ambiguous areas. It took a long time, but having a ground truth classification of surface type will be helpful to studies past our own.

3. Figure 2 (and also Figure 4): Could you please explain the meaning of colors and give a color bar on the side?

The red is clouds and the white is non-clouds. Yes, this should be included in both figures.

4. One of my major concern is that since this work could be potentially used in the EMIT mission, the authors should also consider the impact of dust aerosols. With the three channels selected in this study, it is possible that heavy dust cases were detected as clouds. I strongly suggest the authors use a case study to demonstrate the defined thresholds are also good for aerosols, in particular dust plumes.

This is an astute point, and warrants some additional discussion of the topic in the conclusion. Fortunately EMIT is somewhat immune to this problem because EMIT will not actually measure mineral dust in the atmosphere. It is a geologic mapping mission to map the mineralogy of mineral dust source areas. In fact, the mission intends to filter any AOD550 higher than 0.4. From this perspective, it is fine if the dust plume is screened, because that data would not have been used anyway. Also, it is not necessary that the cloud screening method detect such plumes, because the mission has other methods for estimating AOD550 in the Level 2 stage. By filtering obviously obscured scenes, cloud screening will reduce transmitted data volumes by approximately 50%, enabling EMIT to achieve its geologic mapping objectives in the first 6 months of operation.

5. Please consider cite a recent publication, which developed surface-type based machine learning models for cloud masking and cloud phase classification.

Wang, C., Platnick, S., Meyer, K., Zhang, Z., and Zhou, Y.: A machine-learning-based cloud detection and thermodynamic-phase classification algorithm using passive spectral observations, Atmos. Meas. Tech., 13, 2257–2277, https://doi.org/10.5194/amt-13- 2257-2020, 2020.

Great addition! Thank you.

Global Cloud Property Models for Real Time Triage Onboard Visible-Shortwave Infrared Spectrometers

Macey W. Sandford[1], David R. Thompson[2], Robert O. Green[2], Brain H. Kahn[2], Raffaele Vitulli[3], Steve Chien[2], Amruta Yelamanchili[2], Winston Olson-Duvall[2]

[1]University of Hawai'i at Manoa, Hawai'i Institute of Geophysics and Planetology, Department of Earth Sciences, Honolulu, HI, USA
[2]Jet Propulsion Laboratory, California Institute of Technology, Pasadena, CA, USA
[3]European Space Agency, European Space Research and Technology Center, Noordwijk, Netherlands

Correspondence to: Macey W. Sandford (msandfor@hawaii.edu)

Abstract. New methods for optimizing data storage and transmission are required as orbital imaging spectrometers collect ever-larger data volumes due to increases in optical efficiency and resolution. In Earth surface investigations, storage and downlink volumes are the most important bottleneck in the mission's total data yield. Excising cloud-contaminated data onboard, during acquisition, can increase the value of downlinked data and significantly improve the overall science performance of the mission. Threshold-based screening algorithms can operate at the acquisition rate of the instrument but require accurate and comprehensive predictions of cloud and surface brightness. To date, the community lacks a comprehensive analysis of global data to provide appropriate thresholds for screening clouds or to predict performance. Moreover, prior cloud screening studies have used universal screening criteria that do not account for the unique surface and cloud properties at different locations. To address this gap, we analyzed the Hyperion imaging spectrometer's historical archive of global Earth reflectance data. We selected a diverse subset spanning space (with tropical, midlatitude, arctic, and Antarctic latitudes), time (2005-2017), and wavelength (400 – 2500 nm) to assure that the distributions of cloud data are representative of all cases. We fit models of cloud reflectance properties gathered from the subset to predict locally and globally applicable thresholds. The distributions relate cloud reflectance properties to various surface types (land, water, and snow) and latitudinal zones. We find that taking location into account can significantly improve the efficiency of onboard cloud screening methods. Models based on this dataset will be used to screen clouds onboard orbital imaging spectrometers, effectively doubling the volume of usable science data per downlink. Models based on this dataset will be used to screen clouds onboard NASA's forthcoming mission, the Earth Mineral Dust Source InvesTigation (EMIT).

1 Introduction

Imaging spectrometers, also known as hyperspectral imagers, collect images in the form of three-dimensional data cubes: a two-dimensional image of the target surface in the field of view and swath of the instrument with a continuous spectrum in the third dimension. With the recent decommissioning of Hyperion, an early imaging spectrometer onboard NASA's Earth

Observer 1 (EO-1), many space agencies are now planning or operating a new generation of orbital imaging spectrometer missions, e.g. HISUI (Tachikawa et al., 2012), EMIT (Green et al., 2018), EnMAP (Guanter et al., 2015), CHIME, PRISMA, DESIS, TRUTHS. At the time of this writing, NASA is studying dramatically enhanced imaging spectrometer architectures to provide measurements with global coverage (National Academies of Sciences, Engineering, and Medicine 2018). As instrument capabilities grow, the swath width and length of these instruments permits growing coverage areas. Due to the high dimensional nature of these datasets, the duty cycle of these instruments is expected to be limited by data volume. They are operated with a store-and-forward mode (Williams et al., 2002), where the data are stored onboard in a limited "flight recorder" and transmitted when a ground station is within view or when a manual transfer occurs. This limits the bandwidth from the satellite to the ground and ultimately the total data yield of the mission. Consequently, optimizing the downlink from orbital remote sensing spacecraft can increase the science productivity of these missions. One promising strategy to reduce data volumes involves analyzing images onboard as they are being collected, excising contaminated or irrelevant scenes, and preserving good quality data for preferential storage and downlink (e.g. Thompson et al., 2014; Doggett et al., 2006; and Altinok et al., 2016).

Clouds are the most promising target for onboard screening since they are a common yet unpredictable contaminant that prevents direct observations of surface features. Previous studies indicate that clouds account for over half of the annual sky cover globally (Mercury et al., 2012; Eastman et al., 2011; King et al., 2013; Mace et al., 2009; Rossow and Schiffer, 1999). Thus, onboard cloud screening could approximately double the science productivity per downlink without changing the total stored or transmitted data volumes. Doggett et al. (2006) onboard EO-1 used expert decision tree and support vector machine learning for onboard cloud classification. Altinok et al. (2016) onboard IPEX and Wagstaff et al. (2018) onboard EO-1 used random decision forest machine learning for onboard cloud classification. Though these were not continuous cloud-screening tools, they have determined that cloud screening is in fact a viable solution to the data reduction problem. NASA's EMIT mission has since baselined this capability (Green et al, 2019), and will be the first imaging spectrometer to use continuous onboard cloud screening operationally. These new generation missions will build on a long history of cloud screening algorithms in ground data systems. Most of these screening algorithms treat cloud detection as a classification problem, where attributes of the instrument data are used to determine whether clouds are present. They use a wide variety of techniques including spectroscopically-estimated atmospheric properties (Taylor et al., 2016), band- or regionally-specific threshold tests (Ackerman et al., 1998), spatial variability (Martins et al., 2002), reflectance models of surface and atmosphere (Gómez-Chova et al., 2007), or data-driven machine learning methods (Yhann et al., 1995; Wang et al., 2020). Onboard algorithms carry special requirements: they must be simple, for encoding into instrument hardware or low-power spaceflight computers, and they must use only data available to the spacecraft at the time of acquisition. Finally, because the screened data is irrevocably lost, its behavior should be transparent to the operators and tunable to be more aggressive or conservative depending on their error tolerance. In addition, the algorithm's statistical properties and error rates should be well understood.

Most prior screening approaches, including those designed for onboard use, strive for global performance – a cloud classifier that works the same way for all locations globally. However, the nature of the classification problem changes

depending on location. Neither the coverage nor the spectral appearance of clouds is uniform. Clouds cover more of the oceans (68-72%) on Earth annually than land (54-58%), and tropical regions are exceptionally cloudy (Mercury et al., 2012; Eastman et al., 2011; King et al., 2013; Rossow and Schiffer, 1999). Moreover, cloud optical properties vary regionally due to the different processes involved in their formation and evolution (Thompson et al., 2018). Finally, the optimal thresholds for a particular excision scenario also depend on the expected brightness of the surface (Thompson et al., 2014). Nevertheless, prior studies have relied on universal cloud models and excision criteria, applying the same models for use across the globe. Considering cloud fractions as a function of surface type and latitude could lead to more precise cloud detection. Based on this, we hypothesize that location-specific cloud models can improve performance relative to global methods.

To test this hypothesis, we refine the cloud-screening algorithm previously introduced in Thompson et al. (2014). The original algorithm uses three bands of interest to distinguish clouds from other surface types (El-Araby et al., 2005; Ackerman et al., 1998; Williams et al., 2002; Griffin et al., 2003). This has the desired properties of being simple, fast, transparent, and tunable by ground operators. Here, we analyze the Hyperion global archive to provide globally applicable models that are parameterized by latitude and surface type, enabling reflectance thresholds to predict the classification of cloud-contaminated data and non-cloud-contaminated data (land, water and snow) in new scenes for EMIT and other future orbital missions.

2 Methods

Most cloud screening algorithms are *classifiers* – they analyze independent datapoints and decide which ones should be flagged as cloudy. These individual datapoints can be pixels within a data cube (Altinok et al., 2016), in which case each location is labeled independently. Other algorithms label segments within the scene (Thompson et al., 2014), or entire image cubes. In this study, our datapoints are individual pixels that are single locations within a scene, or image. Each pixel is associated with a complete measured radiance spectrum and each receives an independent classification as either clear or cloudy. We analyzed data from the Hyperion imaging spectrometer, an instrument onboard NASA's EO-1 satellite, which collected a globally representative data set over more than a decade (Thompson et al., 2018).

After calculating TOA reflectance, we labeled each pixel as one of four categories (land, water, snow and clouds), which will be described in further detail in Section 2.2. We then accumulated brightness distributions for each pixel type, describing their respective TOA values in each of the following wavelengths of interest: 447.17 nm, 1245.36 nm, and 1648.90 nm (Thompson et al., 2014). Our procedure took the following steps: we acquired a dataset of representative spectra from a historical data archive; we chose channels or bands that would be used to classify pixels; we calculated pixel brightness distributions for different surface types and latitudes; and finally, we optimized channel thresholds given the distributions and false alarm requirements. These channel thresholds can predict the optimal TOA values for screening clouds in new scenes based on advance knowledge of surface types and viewing geometry.

2.1 The Data Set

The Hyperion instrument was a push broom imaging spectrometer that operated onboard NASA's Earth-Observing One (EO-1) spacecraft from 2000-2017 that followed a polar orbit. It acquired spectra in 220 channels spanning 357 to 2576 nm at approximately 10 nm spectral resolution. Hyperion operated in a targeted acquisition mode, acquiring images at specific locations of interest. Each map was approximately 7.7 km in width, typically 42 km in length with a spatial resolution of 30 m per pixel. During its 17-year operational lifetime, Hyperion acquired tens of thousands of maps across diverse areas including arctic, Antarctic, oceanic, and terrestrial surfaces. We selected a subset of 102 Hyperion images over the entire time range of the mission for our study. To ensure that we sampled the entire globe, we collected approximately 25 images from each section of the globe. The following subsets were included: Tropics (23.5°S to 23.5°N), Arctic (66.5°N to 90°N), Antarctic (66.5°S to 90°S), and Midlatitudes (66.5°S to 23.5°S and 23.5°N to 66.5°N). Most Hyperion data was acquired over land, so we included a subset of longitudes spanning the Pacific Ocean (121°E to 180°E and 121°W to 180°W) to capture the spectral properties of water. We found that there were many less applicable images from both of the polar regions so combining them we included 21 images. We included 30 images from the Tropic region and 51 images from the Midlatitudes. These number are not round because of the issue of resampling when including the Ocean subset. The 19 images in the ocean category can be found in the other latitudinal zones, so any cross over between the two subsets were eliminated to ensure the entire sample set was unique. We transformed the radiance measurements to Top of Atmosphere (TOA) reflectance values to remove the variability caused by solar geometry.

In order to detect cloudy pixels with confidence, we selected three specific spectral bands that can distinguish clouds from other surface types. It is important to note that Earth's total TOA energy flux constitutes the total incoming solar radiation, the consequential outgoing reflected shortwave radiation from the clouds and surface, and the outgoing emitted longwave radiation from Earth's surface, atmosphere, and clouds (e.g., Trenberth et al. 2009). Some other cloud screening algorithms do use longwave channels which provide extra sensitivity to high altitude clouds (Mercury et al., 2014). However, this study sought to discriminate cloud and clear locations using the Visible-ShortWave Infrared (VSWIR) region alone. This made our results directly applicable to future missions measuring solar-reflected wavelengths. We selected three wavelengths of interest, namely 447.17 nm, 1245.36 nm, and 1648.90 nm, based on previous studies distinguishing clouds from land, water, and snow (Ackerman et al., 1998; Griffin et al., 2003; El-Araby et al., 2005; Thompson et al., 2014). Clouds and snow had a high reflectance in the 447 nm band while land and water did not. The near-infrared (1245 nm) and shortwave-infrared (1650nm) band reflectance values effectively discriminated between clouds and snow. Snow had a slightly lower reflectance in the 1245 nm band than clouds while the 1650 nm band showed snow as even less reflective than clouds (Griffin et al., 2003). We used just these three channels, since a small subset of bands enables threshold-based algorithms to be encoded easily into instrument electronics hardware, for real-time execution at the native frame rate of the spectrometer.

2.2 Classification

Accurate ground truth classifications were necessary to define cloud and land statistics for building the classifier. They were also useful for evaluating the resulting model's accuracy by comparing predictions against manual labels. Pixels were hand-labeled using image editing software assure accuracy in classifying each surface type (Fig. 1). The pixels in each image of the sample set were given a color value based on their surface type (land = red, water = blue, cloud = red, snow = cyan, ambiguous = black). We then used these color values to relate the pixels' category of land, water, snow, or clouds to their TOA reflectance values. After fitting this model, the manual classification will be used to verify the model's classification accuracy. We only labeled opaque clouds; all pixels bordering various classification types were labeled as "ambiguous" to avoid misclassification.

After manual labeling, we associated the surface types with the TOA reflectance value in each of the three bands of interest. This association produced three-dimensional frequency distributions of TOA reflectance values based on wavelength and surface type (Fig. 2). They described the conditional probability of a pixel's TOA reflectance value given its classification as cloud or clear sky, c_1 and c_2 respectively ($P(y|c_{1,2})$). The non-cloud distribution contained all non-cloud surface types (land, water, and snow). To assess the classification power over each surface, we tracked the brightness distributions of each surface type independently. To capture the effect of different climates, we represented the distributions as a function of latitudinal zone, P(y|x,c), where x was the zone of interest.

2.3 Algorithms

Our cloud-screening approach predicted scene-specific thresholds in three bands for real-time use onboard (Thompson et al., 2014). Our cloud-screening algorithm defined an exclusion region $R \subseteq \mathbb{R}^d$, i.e. a range of TOA reflectance values for which a pixel was classified as cloudy. In other words, it mapped the pixel brightness values to a binary classification $c = f(\mathbf{y})$: $\mathbb{R}^d \mapsto \{c_1, c_2\}$. A vector y represented the spectrum of the pixel being classified. Thus, the decision rule for this classification was,

$$f(\boldsymbol{y}) = \begin{cases} c_1, \; if \; \boldsymbol{y} \in R \\ c_2, \; if \; \boldsymbol{y} \notin R \end{cases}, \tag{1}$$

where R was defined with a set of thresholds, φ (in this case a triplet). Any pixel exceeding all three thresholds simultaneously is classified as cloud-contaminated (Fig. 3). We then used the following expected loss function, where α_{FP} and α_{FN} were the false positive and negative penalties, respectively,

$$E[\mathcal{L}] = \int_R \alpha_{FP} P(c_1|\boldsymbol{y}, \boldsymbol{x}) d\boldsymbol{y} + \int_{\mathbb{R}^d/R} \alpha_{FN} P(c_2|\boldsymbol{y}, \boldsymbol{x}) d\boldsymbol{y}, \tag{2}$$

A false positive penalty applied to cases where clear pixels were classified as cloud contaminated. $P(y|c_1)$ and $P(y|c_2)$ were the probability of encountering a cloud-contaminated pixel and a clear pixel, respectively. $P(c_1)$ and $P(c_2)$ were the prior probability of clouds and clear sky, respectively, based on an historical average. To eliminate any bias due to historical observations, an "uniformed" prior assigning equal probability to all classes could also be used. Minimizing this function (Eq. 2) produced the optimal threshold for the given conditions defined by **x**. Using Bayes' rule and assuming independence (Thompson et al.,

2014), the expected loss function could be decomposed into the respective likelihoods and priors for the posterior described above,

$$E[\mathcal{L}] = \int_R \alpha_{FP} P(\boldsymbol{y}|\boldsymbol{x}, \boldsymbol{c_1}) P(c_1) d\boldsymbol{y} + \int_{\mathbb{R}^d/R} \alpha_{FN} P(\boldsymbol{y}|\boldsymbol{x}, \boldsymbol{c_2}) P(c_2) d\boldsymbol{y}, \quad (3)$$

Thus, we could use the likelihood, or sampling distribution, created from the Hyperion sample set to minimize our expected loss and produce predictive thresholds for screening. As in Thompson et al. (2014), we represented probability distributions through histogram counts, creating a 3D table with one dimension for each of the three wavelengths. This allowed a fast-recursive calculation of equation (3) when searching over thresholds. For a given false positive penalty, we searched over all possible thresholds and selected the one which produced the lowest effective loss.

3 Results

The globally representative sample set of imaging spectroscopy data provides a comprehensive sample of TOA reflectance for various surface types in space, time, and wavelength as well as a prediction model for screening cloud-contaminated data onboard orbital imaging spectrometers. This section discusses our findings concerning excision thresholds, cloud brightness, the potential improvement yield of downlink using the cloud-screening algorithm, a comparison of resulting cloud fractions in our data set with previous literature, justifying the empirical error of our data set, and the implications of our study and cloud-screening tool for future missions.

3.1 Cloud Screening Thresholds

The model used for cloud screening was developed using cloud brightness distributions in TOA values as a function of time, space, and wavelength. The brightness distributions collected from the Hyperion sample set represent cloud and non-cloud brightness values in TOA units, for each band (447.17 nm, 1245.36 nm, 1648.90 nm). The sample set scenes cover representative regions across the globe (Table 1).

The output of the algorithm was a threshold triplet that defined the exclusion region, i.e. the minimum TOA reflectance values of opaque cloud-contaminated data (discussed in Sect. 2.3). The penalties in the expected loss function determined our tolerance for errors; a higher false positive penalty led to a more conservative threshold and a smaller exclusion region. As we hypothesized, we were able to improve performance further by considering the expected surface properties when defining the exclusion region. For example, since clouds and snow had similar reflective properties in two of the bands used, snow scenes were most challenging and dominated the threshold criterion. Consequently, one could use a more aggressive threshold triplet to screen clouds outside Arctic regions, improving performance without incurring misclassifications. The result of a conservative threshold (α_{FP}=1000) calculation, a moderate threshold (α_{FP}=100) calculation, and an aggressive threshold (α_{FP}=10) calculation are shown in a two-dimensional histogram representing all scenes in the sample set (Fig. 4).

The optimal thresholds, where the loss was minimized, at various false positive rates using the Hyperion sample set are shown in Table 2. The thresholds were defined differently for each latitudinal zone. Sect. 3.4 describes the statistical

validation tests we used to ensure the size and breadth of our subset, or sampling distribution, was sufficient to predict these thresholds for future scenes.

3.2 Cloud Brightness

The Hyperion global data set was sampled and manually classified to understand cloud brightness as a function of time, space, and wavelength. We collected the TOA values in a 3-dimensional histogram, one axis for each wavelength studied. This produced a probability distribution of TOA values of clouds globally that we used to predict the classification of TOA values for future scenes. In order to verify if classifying clouds depending on their latitudinal zone would produce a lower false alarm rate, we subset our scenes based on latitude and surface type.

Table 3 presents the mean TOA reflectance values for each latitudinal zone and wavelength. Cloudy pixels had higher TOA reflectance values while non-cloudy pixels had generally lower TOA values (Fig. 3). We found our data to align with the general properties of non-cloud surface types discussed in Ackerman et al. (1998). Specifically, pixels with snow had low TOA reflectance values at 1250 nm and even lower TOA reflectance values at 1650 nm, while having high TOA reflectance properties at 447 nm.

Separating cloud brightness values as a function of latitude is also helpful in determining the type of clouds formed in each region (Oreopoulos et al. 2014), although this is not included in our study. Studying these TOA reflectance value distributions for opaque cloud cover will be helpful to understand shortwave albedo at regional and global scales. For example, opaque clouds compose a smaller percentage of global cloud cover with respect to transparent or spatially heterogeneous clouds (e.g., Rossow and Schiffer 1999; Stubenrauch et al. 2017) but deep convective clouds have an outsized influence on Earth's TOA radiative budget and hydrological cycle in the tropical latitudes (e.g., Jakob and Tselioudis 2003; Tan et al. 2015).

3.3 Empirical Error Tests

This section evaluates the stability of the threshold estimation approach and then quantifies cloud excision performance. Based on parameters such as latitude and surface type, we determined the false positive and false negative performance for different observing conditions. Screening classification depended largely on the false positive parameter (Fig. 5).

It was critical that any threshold set generalized to new scenes not yet seen. While an infinitely large dataset would be sure to capture the real statistics of the globe, we were necessarily limited in the number of scenes used in the analysis. To confirm this dataset was sufficiently representative to produce general thresholds, we performed two validation tests. First, we performed a leave-one-out cross-validation experiment, recalculating cloud-screening thresholds 102 times and excluding a different scene for validation from each trial. Every test conducted resulted in the same thresholds presented in Table 2. This stability is one validation that the optimal margin for the distribution for the brightness resolution of our lookup table was not sensitive to "outlier" cases but rather responded to the true statistics of global clouds. More generally, it confirmed that our dataset was sufficient in space, time and wavelength to predict optimal thresholds for future scenes.

In the second test, we conducted an experiment to measure the variance of the cloud-screening threshold estimates using bootstrap techniques. The 102 images used in the initial experiment were used to create a sample set through sampling with replacement 500 unique times. Data concerning the threshold calculation were recorded each of the 500 times. Of particular interest is the variance in threshold calculation for each latitudinal zone (Table 5). The variance in each latitudinal zone was low, showing that our estimation approach was robust.

3.4 Potential Improvement Yield of Screening

To evaluate the utility of cloud screening in terms of imaging spectroscopy science investigations, we analyzed the improvement yield for two specific cases of future orbital imaging spectrometers. We simulated the data return with and without the use of onboard cloud screening.

Our first case study used the orbital parameters of the Earth Surface Mineral Dust Source InvesTigation (EMIT) mission (Green et al., 2018). EMIT will use a visible to short wavelength infrared (VSWIR) imaging spectrometer to map the mineralogy of mineral-dust forming regions worldwide. This will improve our understanding of the mineral composition of airborne dust particles, informing the Earth System Models that simulate the dust cycle. Understanding the composition of mineral dust in Earth's atmosphere will in turn provide insight into the impact of dust on direct radiative forcing in Earth's climate. The EMIT mission will be launched to the International Space Station in 2021, with an orbit dominated by low-latitude regions. It intends to use data under clear-sky conditions without significant aerosol loading, and filter scenes with an Aerosol Optical Depth (AOD) greater than 0.4 at 550 nm. The Hyperion dataset is broadly representative of these atmospheric conditions. A case study for EMIT provides one example of the potential for onboard cloud-screening (Table 6). Since the EMIT mission plan does not entail collecting data over the latitudinal zone specified as Ocean, we ignored that region in the case study.

We intersected the EMIT coverage area with historical cloud probability maps to assess the potential improvement for the instrument (Yelamanchili et al., 2019, Chien et al., 2019). We simulated cloud cover fractions using pre-calculated global cloud probabilities (x) from historical MODIS data (Mercury et al., 2012), defined as an annual average cloud cover probability at a spatial resolution of one degree. Then we simulated ISS observations at a 10 second rate for one year, starting on February 1st, 2022. The large improvement indicated the value of screening cloud-contaminated data. For the cloud screening approach in this work, we predicted at least double the current return of useful data in each latitudinal zone, and for the mission overall. There is a notable difference in yield when considering all regions at once and when considering one region at a time. Some areas of the globe are cloudier than others, so the benefit of using a cloud-screening tool is particular to the region(s) of interest and the sampling strategy of each mission.

As previously discussed, past literature presents cloud cover fractions that are greater over land than water and that tropical regions are more cloudy than other latitudinal zones (Eastman et al., 2012, Ackerman et al., 1998). The EMIT case study cloud fractions showed that cloud cover in the tropics was greater than any other region studied. Due to the nature of our

latitudinal zone sorting, we could not directly compare the Ocean cloud cover fractions with land cloud cover fractions; the other latitudinal zones could also have contained regions associated with Oceans.

CHIME (Copernicus Hyperspectral Imaging Mission for the Environment) is an ESA (European Space Agency) mission that aims to provide routine hyperspectral observations of the Earth to aid in management of natural resources, assets and benefits for the European Union. One main aspect of CHIME's technological advances is to facilitate increased field of view (>5 deg) observations and low spatial sampling (< 30 m) with a high data rate (>1 Gbit/s) processor onboard the instrument. In light of this requirement, an onboard processing architecture such as a cloud screening algorithm is valuable to the CHIME mission.

The CHIME team conducted a simulated study, comparable to EMIT, where they reported simulated cloud cover based on one orbital cycle (223 orbits over 15 days) for summer 2012 with meteorological statistical inputs for cloud coverage simulation. The preliminary results of this study revealed that with a cloud screening algorithm onboard, CHIME would experience about a 50% increase in useable data (Table 6). In summary, both of the case studies considered facilitated at least double the return of viable data for each mission's desired objective.

4 Discussion and Conclusion

The method described for screening cloud-contaminated data onboard orbital imaging spectrometers will at least double the volume of useful data for a fixed downlink size. We collected and studied a globally representative data set, producing optimal screening thresholds based on latitudinal zones. Using latitude as a parameter in screening clouds will help correctly classify cloud-contaminated pixels while reducing misclassifications of other surface types. The overall yield of useful data doubles when using the screening algorithm. In addition, we have produced a representation of cloud brightness in the 447.17 nm, 1249.36 nm, and 1650.90 nm wavelength bands, changing with latitude and surface type, based on TOA reflectance values.

Our results showed that mean cloud TOA brightness differed in the bands studied as a function of latitudinal zone and surface type; Tropics, Arctic, Antarctic, Midlatitudes, and Pacific Ocean areas (Table 4). The starkly higher differences seen in the Arctic region show that this region needed more conservative thresholds than a global "universal" model which did *not* calculate unique screening thresholds based on latitude. The difference in these mean values indicates that the optimal thresholds assigned for the classification of clouds in each area should also differ (Table 2).

Given the relatively low complexity and risk involved in implementing onboard cloud screening, it is a valuable option available to mission designers trying to achieve higher yield at low cost. It can be incorporated directly into instrument hardware, saving the storage costs of downlinking cloudy data. Its operation can be tuned over time, if needed, to obtain optimal performance for the specific observing profile of the mission. Even a very conservative threshold, with almost no probability of excising good data, can significantly reduce data volumes (Thompson et al., 2014). For this reason, the EMIT mission (Green et al., 2018) will use this cloud screening method to optimize its downlink within the allowable resources provided by its position on the International Space Station. Its observation plan, which targets arid regions in the midlatitude

and tropical latitudes, can use more aggressive thresholds without risking error due to snow cover. The data accumulated over its year-long mission will provide independent validations on these thresholds and brightness distributions.

The methods suggested for cloud screening in this article as with Thompson et al. (2014) rely only on TOA reflectance and thresholding. Even alternative methods flown on EO-1 (Wagstaff et al., 2018) and IPEX (Altinok et al., 2016) using random decision forests are only slightly more computational demanding (impacted by the size of the trees, number of trees voting, and neighborhood used to inform the classification). Current imaging spectrometers produce data at high rates (Giga bits per second). However, because classifiers are only likely to use a small number of spectral bands only a smaller amount of data needs to be processed on the fly, making next generation conventional processors viable. In addition, space missions are flying alternative processors that would provide dramatically enhanced computation: the IPEX Cubesat flew a Gumxtix Overa (Chien et al., 2017), The Mars Helicopter (Grip et al., 2019) will fly a Qualcomm Snapdragon, and the ESA FSSCCAT Cubesat (ESA 2020) will fly an Intel Myriad Processor. Although, future computing needs for onboard will continue to grow (Dally et al., 2020) well beyond these flights.

The results of this work also have applications outside screening clouds onboard imaging spectrometers. Conversely, collecting solely cloud contaminated data that is identified using the algorithm described in this paper can aid in an instrument's stray light correction or other data products. On the other hand, the global study of cloud brightness shown in this paper has the potential to be used in various cloud studies, for example those concerning cloud type and subsequent brightness as a function of latitudinal zone (Oreopoulos et al. 2014).

Acknowledgements

A portion of this research was performed at the Jet Propulsion Laboratory, California Institute of Technology (JPL). We acknowledge the support of the National Aeronautics and Space Administration (NASA). The NASA JPL summer internship program and the Imaging Spectroscopy group at JPL supported this work. Amruta Yelamachili and her colleagues at JPL helped to support the EMIT case study. Raffaele Vitulli and his colleagues at ESA helped to support the CHIME case study.

References

Ackerman, S. A., Strabala, K. I., Menzel, W. P., Frey, R. A., Moeller, C. C., and Gumley, L. E.: Discriminating clear sky from clouds with MODIS. J. Geophys. Res., Atmosp., vol. 103, no. D24, pp. 32 141–32 157, 1998.

Altinok, A., Thompson D.R., Bornstein B., Chien S.A., Doubleday J., Bellardo J., "Real-Time Orbital Image Analysis Using Decision Forests, with a Deployment Onboard the IPEX Spacecraft." Journal of Field Robotics, 33(2):187-204, 2016.

Chien, S., Doubleday, J., Thompson, D. R., Wagstaff, K. L., Bellardo, J., Francis, C., Baumgarten, E., Williams, A., Yee, E., Stanton, E., Piug-Suari, J. Onboard autonomy on the intelligent payload experiment cubesat mission. Journal of Aerospace Information Systems. 2017 Jun;14(6):307-15.

Chien, S., Yelamanchili, A., and Doubleday, J.: Policy-based automated science coverage scheduling for earth science mission analysis and operations (NISAR, ECOSTRESS, OCO-3, and EMIT). Earth Science Technology Forum (ESTF 2019), Moffett Field, California, USA, June 2019.

Dally, W. J., Yatish, T., and Song, H. "Domain-specific hardware accelerators." Communications of the ACM 63.7 (2020): 48-57.

Doggett T., Greeley R., Chien S., Castano R., Cichy B., Davies A.G., Rabideau G., Sherwood R., Tran D., Baker V., Dohm J.: Autonomous detection of cryospheric change with hyperion on-board Earth Observing-1. Remote Sensing of Environment, 30;101(4):447-62, 2006.

Eastman, R., Warren, S., and Hahn C.: Variations in cloud cover and cloud types over the ocean from surface observations, 1954–2008. J. Climate, vol. 24, no. 22, pp. 5914–5934, 2011.

El-Araby, E., Taher, M., El-Ghazawi, T., and Le Moigne, J.: Prototyping automatic cloud cover assessment (ACCA) algorithm for remote sensing on-board processing on a reconfigurable computer. Proc. IEEE Int. Conf. Field-Programm. Technol., pp. 207–214, 2005.

Gómez-Chova, L., Camps-Valls, G., Calpe-Maravilla, J., Guanter, L., & Moreno, J.: Cloud-screening algorithm for ENVISAT/MERIS multispectral images. IEEE Transactions on Geoscience and Remote Sensing, 45(12), 4105-4118. 2007.

Green, R., Mahowald, N., Thompson, D., Clark, R., Ehlmann, B., Ginoux, P., Kalashnikova, O., Miller, R., Okin, G., Painter, T. and Perez, C.: The Earth Surface Mineral Dust Source Investigation Planned for the International Space Station. Geophysical Research Abstracts (Vol. 21), 2019.

Green, R.O., Mahowald, N. M. , Clark, R. N., Ehlmann, B. L., Ginoux, P. A., Kalashnikova, O. V., Miller, R. L., Okin, G. S., Painter, T. H., García-Pando, C. P., Realmuto, V. J., Swayze, G. A., Thompson, D. R., Middleton, E., Guanter, L., Dor, E. B. and Phillips, B. R.: NASA’s Earth Surface Mineral Dust Source Investigation. AGU Fall Meeting, Washington D.C., 10-14 Dec, 2018, A24D-01, 2018.

Griffin, M. K., Burke, H. K., Mandl, D., and Miller, J.: Cloud cover detection algorithm for EO-1 hyperion imagery. Proc. 17th SPIE AeroSense Conf. Algorithms Technol. Multispectral, Hyperspectral Ultraspectral Imagery IX, Orlando, FL, USA, 2003.

Grip, H. F., Lam, J., Bayard, D.S., Conway, D.T., Singh, G., Brockers, R., Delaune, J.H., Matthies, L. H., Malpica, C., Brown, T. L., Jain, A. Flight Control System for NASA's Mars Helicopter. In AIAA Scitech 2019 Forum 2019 (p. 1289).

Guanter, L., Kaufmann, H., Segl, K., Foerster, S., Rogass, C., Chabrillat, S., Kuester, T., Hollstein, A., Rossner, G., Chlebek, C., Straif, C., Fischer, S., Schrader, S., Storch, T., Heiden, U., Mueller, A., Bachmann, M., Mühle, H., Müller, R., Habermeyer, M., Ohndorf, A., Hill, J., Buddenbaum, H., Hostert, P., van der Linden, S., Leitão, P., Rabe, A., Doerffer,

R., Krasemann, H., Xi, H., Mauser, W., Hank, T., Locherer, M., Rast, M., Staenz, K., Sang, B.: The EnMAP Spaceborne Imaging Spectroscopy Mission for Earth Observation., Remote Sens., 7(7), 8830-8857, doi: 10.3390/rs70708830, 2015.

Jakob, C., and G. Tselioudis: Objective identification of cloud regimes in the tropical western Pacific. Geophys. Res. Lett., 30, 2082, https://doi.org/10.1029/2003GL018367, 2003.

King, M., Platnick, S., Menzel, W., Ackerman, S., and Hubanks, P.: Spatial and temporal distribution of clouds observed by MODIS onboard the Terra and Aqua satellites. IEEE Trans. Geosci. Remote Sens., vol. 51, no. 7, pp. 3826–3852, 2013.

Mace, G. G., Q. Zhang, M. Vaughan, R. Marchand, G. Stephens, C. Trepte, and D. Winker: A description of hydrometeor layer occurrence statistics derived from the first year of merged Cloudsat and CALIPSO data. J. Geophys. Res., 114, D00A26, doi:10.1029/2007JD009755, 2009.

Martins, J. V., Tanré, D., Remer, L., Kaufman, Y., Mattoo, S., & Levy, R.: MODIS cloud screening for remote sensing of aerosols over oceans using spatial variability. Geophysical Research Letters, 29(12), MOD4-1, 2002.

Mercury, M., Green, R. O., Hook, S., Oaida, B., Wu, W., Gunderson, A., and Chodas, M.: Global cloud cover for assessment of optical satellite observation opportunities: A HyspIRI case study. Remote Sens. Environ., vol. 126, pp. 62–71, 2012.

National Academies of Sciences, Engineering, and Medicine.: Thriving on Our Changing Planet: A Decadal Strategy for Earth Observation from Space. Washington, DC: The National Academies Press., doi:10.17226/24938, 2018.

Oreopoulos, L., Cho, N., Lee, D., Kato, S., and Huffman, G. J.: An examination of the nature of global MODIS cloud regimes. J. Geophys. Res. Atmos., 119, 8362–8383, doi:10.1002/2013JD021409, 2014.

Rossow, W. B., and R. A. Schiffer: Advances in understanding clouds from ISCCP. Bull. Amer. Meteor. Soc., 80, 2261–2288, https://doi.org/10.1175/1520-0477, 1999.

Salomonson, V. V. and Appel, I.: Estimating fractional snow cover from MODIS using the normalized difference snow index. Remote Sens. Environ., vol. 89, no. 3, pp. 351–360, 2004.

Stubenrauch, C. J., Feofilov, A. G., Protopapadaki, S. E., and Armante, R.: Cloud climatologies from the infrared sounders AIRS and IASI: strengths and applications. Atmos. Chem. Phys., 17, 13625–13644, https://doi.org/10.5194/acp-17-13625-2017, 2017.

Tachikawa, T., Kashimura, O., Tanii, J., Iwasaki, A., Matsunaga, T., Tsuchida, S., Yamamoto, H.: Outline and Prospect of Hyperspectral Imager Suite (HISUI). Journal of The Remote Sensing Society of Japan, Vol. 32 No. 5, pp: 280-286, 2012.

Tan, J., Jakob, C., Rossow, W., and Tselioudis, G.: Increases in tropical rainfall driven by changes in frequency of organized deep convection. Nature, 519, 451–454, doi: https://doi.org/10.1038/nature14339, 2015.

Taylor, T. E., O'Dell, C. W., Partain, P. T., Cronk, H. Q., Nelson, R. R., Rosenthal, E. J., Chang, A. Y., Fisher, B., Osterman, G. B., Pollock, R. H., Crisp D., Eldering A., and Gunson, M. R.: Orbiting Carbon Observatory-2 (OCO-2) cloud

screening algorithms: Validation against collocated MODIS and CALIOP data. Atmospheric Measurement Techniques, 9(3), 973, 2016.

Thompson, D. R., Kahn, B. H., Green, R. O., Chien, S. A., Middleton, E. M., Tran, D. Q.: Global Spectroscopic Survey of Cloud Thermodynamic Phase at High Spatial Resolution, 2005–2015. Atmospheric Measurement Techniques, vol. 11, no. 2, pp. 1019–1030., doi:10.5194/amt-11-1019-2018, 2018.

Thompson, David R., Green, R. O., Keymeulen, D., Lundeen, S. K., Mouradi, Y., Nunes, D. C., Castano, R., Chien, S. A.: Rapid Spectral Cloud Screening Onboard Aircraft and Spacecraft. IEEE Transactions on Geoscience and Remote Sensing, vol. 52, no. 11, pp. 6779–6792., doi:10.1109/tgrs.2014.2302587, 2014.

Trenberth, K. E., J. T. Fasullo, and J. Kiehl.: Earth's global energy budget. Bull. Amer. Meteor. Soc., 90, 311–324, https://doi.org/10.1175/2008BAMS2634.1, 2009.

Wagstaff, K., Chien, S., Altinok, A., Rebbapragada, U., Thompson, D., Schaffer, S., and Tran, D.: Cloud Filtering and Novelty Detection using Onboard Machine Learning for the EO-1 Spacecraft. International Symposium on Artificial Intelligence, Robotics, and Automation for Space (ISAIRAS 2018), Madrid, Spain, 2018 July, 2018.

Wang, C., Platnick, S., Meyer, K., Zhang, Z., and Zhou, Y.: A machine-learning-based cloud detection and thermodynamic-phase classification algorithm using passive spectral observations, Atmos. Meas. Tech., 13, 2257–2277, https://doi.org/10.5194/amt-13- 2257-2020, 2020.

Williams, J. A., Dawood, A. S., and Visser, S. J.: FPGA-based cloud detection for real time onboard remote sensing. Proc. IEEE Int. Conf. Field-Programm. Technol., pp. 110–116, 2002.

Yelamanchili, A., Chien, S., J.Russino; Wells, C., Green, R., Oaida, B., and Thompson, D. R.: Mission Analysis for EMIT using Automated Coverage Scheduling. Earth Science Technology Forum (ESTF 2019), Moffett Field, California, USA, 2019 June, 2019.

Yhann, S. R., & Simpson, J. J.: Application of neural networks to AVHRR cloud segmentation. IEEE transactions on geoscience and remote sensing, 33(3), 590-604, 1995.

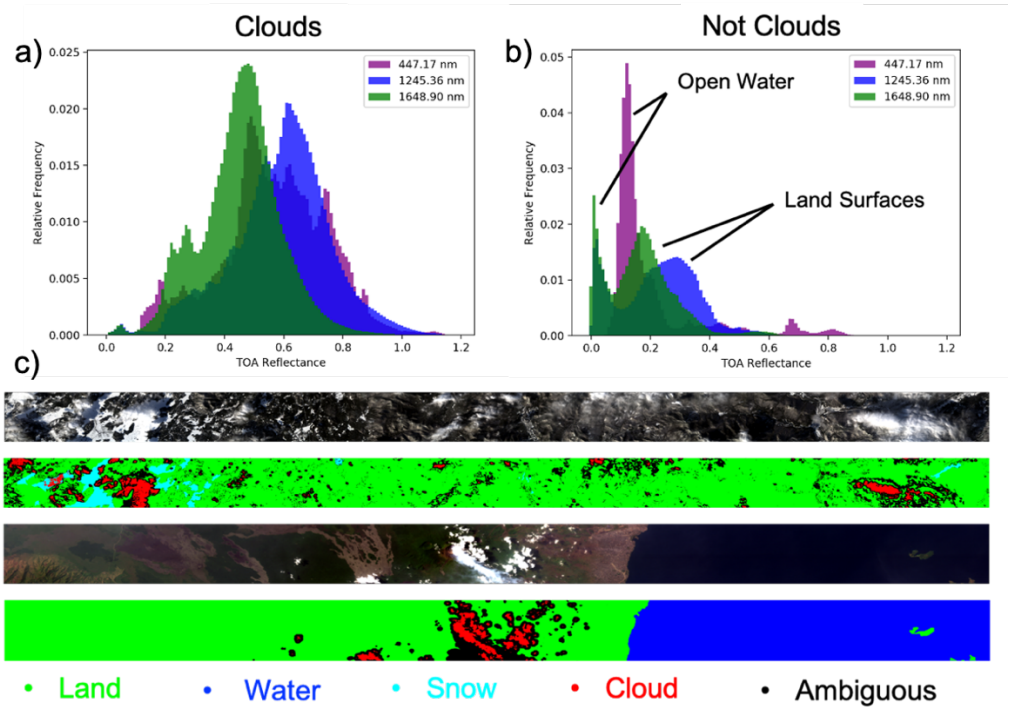

Figure 1: An example of the one-dimensional distributions of a) cloudy and b) non-cloudy pixels in each wavelength created from c) the hand-labeled pixels in the Hyperion images used as ground truth.

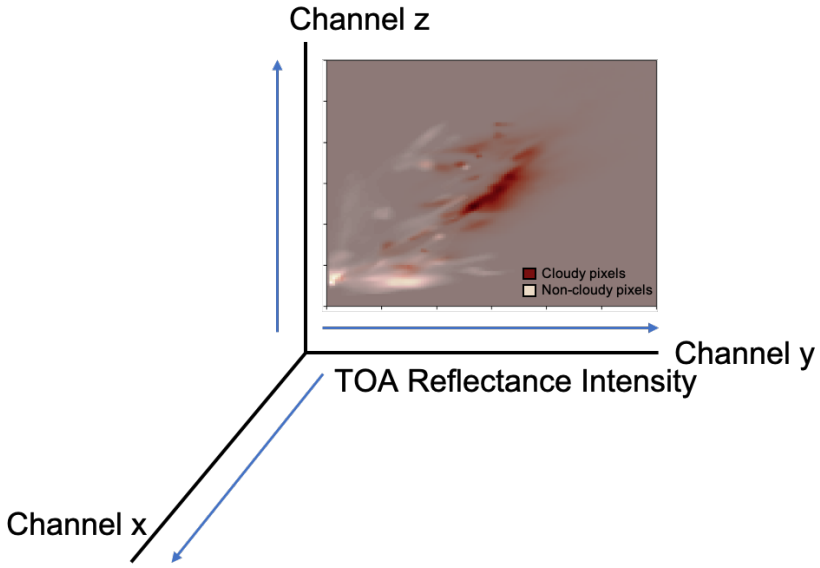

405 **Figure 2: A schematic of the three-dimensional cloud and non-cloud brightness distributions, with an example of a marginal distribution in one plane.**

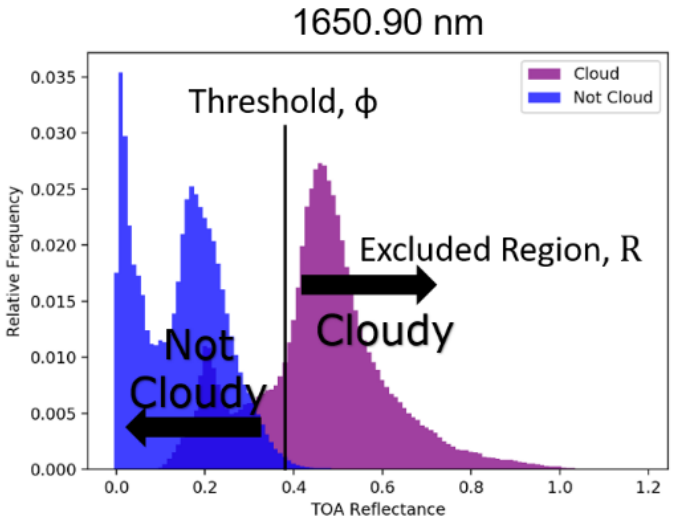

Figure 3: Depiction of the exclusion region used to classify cloud-contaminated data.

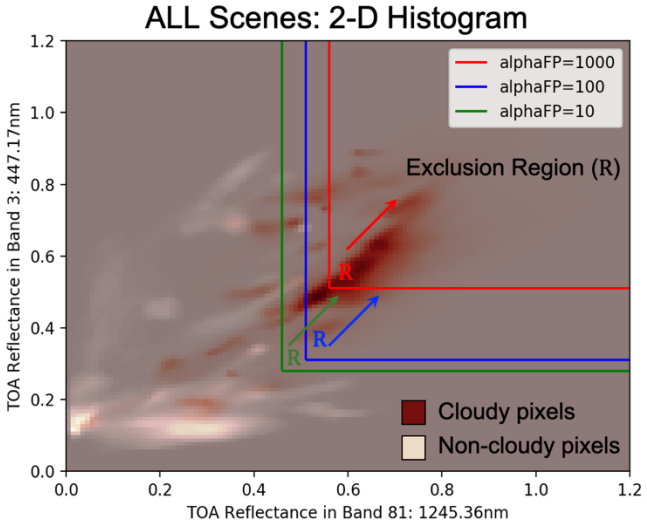

Figure 4: A Two-dimensional histogram of cloud and non-cloud distributions for the Hyperion subset. The color gradient indicates relative frequency. The exclusion region for various false positives are shown as colored rectangles; αFP=1000 (red), αFP=100 (blue), αFP=10 (green).

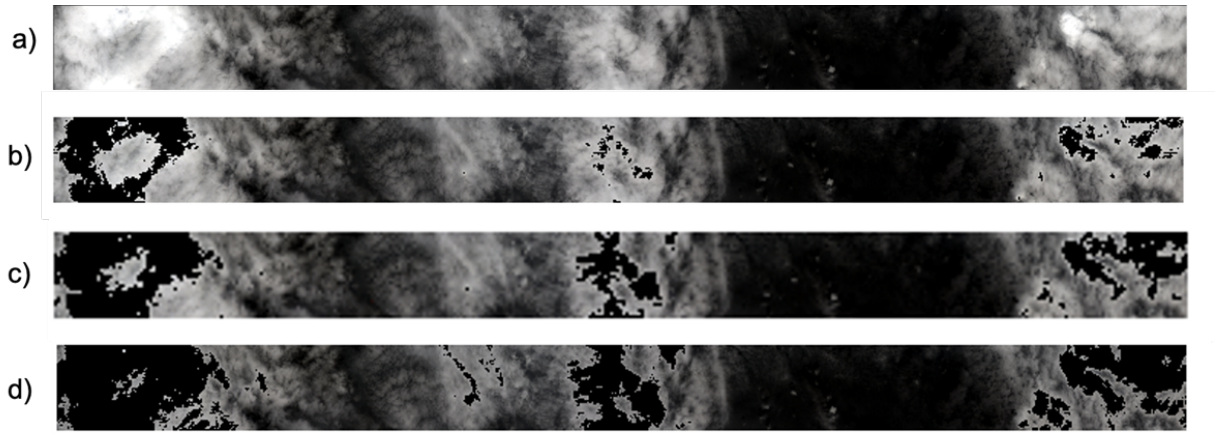

Figure 5: An example of pixels classified as cloudy being excised from a Hyperion image (EO1H1940712011304110T1). These images were created using the default RGB wavelengths in the ENVI program, although the algorithm to create the sub-images in this figure only considers the three wavelengths used in our thresholds. The sub-images show the following, a) the raw image with no screening, b) cloud-screening with αFP=1000 where 8.5 % of the total pixels were excised, c) cloud-screening with αFP=100 where 16.4 % of the total pixels were excised, and d) cloud-screening with αFP=10 where 25 % of the total pixels were excised.

Table 1: The number of images in the Hyperion sample set (102 images) collected in each latitudinal zone. The ocean category also includes images taken in the regions of tropics, midlatitudes, and arctic.

Hyperion Image Sample Set Breakdown

Latitudinal Zone	Number of Images
Tropics	30
Midlatitudes	51
Arctic	21
ALL	102
Ocean Subset	19

Table 2: Optimal Thresholds in TOA (Top of Atmosphere) reflectance values using three difference false positives and a false negative of 1 for each latitudinal zone.

Optimal Thresholds for Screening Clouds

False Positive Value	Latitudinal Zone	447.17 nm	1245.90 nm	1649.36 nm
1000	Tropics	0.31	0.34	0.13
	Midlatitudes	0.52	0.36	0.24
	Arctic	0.47	0.57	0.30
	Ocean	0.41	0.37	0.30
	ALL	**0.51**	**0.56**	**0.29**

	Tropics	0.27	0.25	0.13
	Midlatitudes	0.31	0.51	0.23
100	Arctic	0.55	0.27	0.22
	Ocean	0.39	0.34	0.28
	ALL	**0.31**	**0.51**	**0.22**
	Tropics	0.26	0.21	0.11
	Midlatitudes	0.28	0.45	0.22
10	Arctic	0.54	0.26	0.20
	Ocean	0.32	0.25	0.22
	ALL	**0.28**	**0.46**	**0.22**

Table 3: Mean values of the distributions of TOA reflectance for each classification type, in each wavelength. The change in values across this table verifies the advantage of presenting screening thresholds as a function of latitude.

Cloud Brightness mean values (TOA reflectance)

Latitudinal Zone	447.17 nm	1245.36 nm	1650.90 nm
Tropics	0.47	0.61	0.50
Midlatitudes	0.57	0.61	0.45
Arctic	0.75	0.47	0.45
Ocean	0.49	0.49	0.44
ALL	0.49	0.61	0.48

Table 4: Difference in mean values of the TOA reflectance thresholds in each zone from the overall thresholds. These differences are calculated by using the mean value in each band for the ALL category and subtracting the mean of each zone individually from this value.

Difference in Mean for Subset Latitudinal Zones vs ALL

Latitudinal Zone	447.17 nm	1245.36 nm	1650.90 nm
Tropics	0.02	0	-0.02
Midlatitudes	-0.08	0	0.03
Arctic	-0.26	0.14	0.03
Ocean	0	0.12	0.04

Table 5: Variance in thresholds used to screen clouds based on bootstrapping the thresholds calculations described in the initial experiment 500 times. The variance is presented as a percentage of the mean of the particular zone. The false positive setting was $\alpha FP=1000$ and the false negative $\alpha FN=1$.

Variance in Thresholds from Bootstrapping (% of Mean)

Latitudinal Zone	447.17 nm	1245.36 nm	1650.90 nm
ALL	1.63%	1.77%	0.58%
Tropics	0.30%	1.82%	1.28%
Arctic	1.08%	2.74%	1.96%
Midlatitudes	1.29%	0.87%	0.52%
Ocean	0.60%	1.26%	0.89%

435

Table 6: A case study of EMIT (Earth Surface Mineral Dust Source Investigation) concerning a global cloud fraction simulation was used to determine the improvement yield of the cloud-screening tool in terms of latitude.

Improvement Yield based on Case Studies

Case Study	Simulated Cloud Coverage Observed (%)	Improvement Yield (Factor of increase in usable data)
EMIT	Tropics: 65%	x2.38
	Midlatitudes: 57%	x2.85
	Arctic: 52%	x2.32
	Antarctic: 50%	x2.08
	All Zones: 58%	**x2.04**
CHIME	**All Zones: ~ 50%**	**x2.00**